

Interfacing the Urban Land–Atmosphere System Through Coupled Urban Canopy and Atmospheric Models

Jiyun Song · Zhi-Hua Wang

Received: 1 April 2014 / Accepted: 28 October 2014 / Published online: 19 November 2014
© Springer Science+Business Media Dordrecht 2014

Abstract We couple a single column model (SCM) to a cutting-edge single-layer urban canopy model (SLUCM) with realistic representation of urban hydrological processes. The land-surface transport of energy and moisture parametrized by the SLUCM provides lower boundary conditions to the overlying atmosphere. The coupled SLUCM–SCM model is tested against field measurements of sensible and latent heat fluxes in the surface layer, as well as vertical profiles of temperature and humidity in the mixed layer under convective conditions. The model is then used to simulate urban land–atmosphere interactions by changing urban geometry, surface albedo, vegetation fraction and aerodynamic roughness. Results show that changes of landscape characteristics have a significant impact on the growth of the boundary layer as well as on the distributions of temperature and humidity in the mixed layer. Overall, the proposed numerical framework provides a useful stand-alone modelling tool, with which the impact of urban land-surface conditions on the local hydrometeorology can be assessed via land–atmosphere interactions.

Keywords Land–atmosphere interactions · Land-use land-cover changes · Single column atmospheric model · Urban canopy model · Urban planning

1 Introduction

The world is undergoing rapid urbanization with the percentage of the world’s population in urban areas increasing from 30 % in 1950 to 47 % in 2000, and projected to rise to 60 % by 2030 (Collier 2006; UN 2012). The rapid growth and the associated landscape modification of urban areas necessarily modify the surface energy and moisture balance by altering key physical and biophysical properties, with impacts on local and regional hydroclimate (Arnfield 2003), leading to potential global climate responses via a cascade of land–atmosphere

J. Song · Z.-H. Wang (✉)
School of Sustainable Engineering and the Built Environment, Arizona State University,
Tempe, AZ 85287, USA
e-mail: zhwang@asu.edu

interactions (Niyogi et al. 2009). Urban land-use land-cover (LULC) changes, with modified surface geometric and hydrothermal properties compounded by anthropogenic heat and moisture sources, contribute to numerous urban environmental features such as the urban heat island (UHI), air pollution, and convective rainfall initiation (Taha 1997; Collier 2006).

To assess the impacts of LULC changes, land–atmosphere coupling has been utilized in atmospheric general circulation models (e.g. Yang 1995; Bonan et al. 2002) and regional climate models, such as the Weather Research and Forecasting (WRF) model (Skamarock and Klemp 2008; Trier et al. 2011; Chen et al. 2011). In these models, a major source of uncertainty exists in the parametrization of the surface heat and moisture budgets (Chen and Avissar 1994; Chen and Dudhia 2001; Trier et al. 2011). In addition, due to the unique characteristics of built terrains, e.g. spatial heterogeneity, a modified turbulence field and modified surface energy balance (Wang et al. 2011b), a scalable urban land–atmosphere coupling framework, analogous to the “big canyon” representation for building arrays (Nunez and Oke 1977), is appropriate for studying the direct impact of urban LULC changes.

To parametrize urban land-surface processes, numerous urban canopy models (UCMs) have been developed and widely used in the last decade. Broadly, there are two groups of UCMs, including the single-layer urban canopy model (SLUCM) (Masson 2000; Kusaka et al. 2001; Wang et al. 2013) that focuses on the parametrization of the surface energy budget, and the more complex multilayer UCMs that also capture the momentum transport in urban canopies (Martilli et al. 2002; Dupont et al. 2004; Kondo et al. 2005). Up to date, most UCMs are capable of resolving the vertical transport of energy and sensible heat and predicting surface temperatures realistically, but are inadequate in representing the water transport due to the oversimplification of urban hydrological processes (Grimmond et al. 2010, 2011). Recently, an improved SLUCM including an urban hydrologic model has been developed by Wang et al. (2013), which enables a more realistic representation of evapotranspiration, infiltration, irrigation, and soil moisture states in urban areas and improves the prediction of latent heat fluxes.

Above a built environment, a single column model (SCM) (Troen and Mahrt 1986; Holtslag and Moeng 1991; Noh et al. 2003) can be used to predict the time evolution and spatial distribution of temperature and humidity in the overlying atmospheric boundary layer (ABL). The SCM is a relatively simple representation of the convective boundary layer (CBL) and can faithfully capture the growth of the boundary-layer. It has been found that the boundary-layer growth is sensitive to land-surface characteristics such as evaporation (Troen and Mahrt 1986), which necessitates the need for a realistic representation of the surface states (temperature, soil moisture, sensible and latent heat fluxes). In addition, the entrainment process at the top of the ABL also plays an important role in regulating boundary-layer growth and depends largely on the buoyancy flux, with significant contributions from, e.g. the latent heat flux (Hong et al. 2006).

In this study, we integrate a single column atmospheric model to the latest SLUCM including an improved urban hydrological module (Wang et al. 2011a, 2013; Sun et al. 2013a). The coupled SLUCM–SCM framework is capable of predicting the urban surface energy and water budgets with improved accuracy. Using the proposed model, a range of scenarios of urban LULC changes can be simulated, and their impact on the boundary-layer growth and temperature/humidity distribution under convective conditions assessed.

The paper is organized as follows: an introduction to parametrization schemes in the SLUCM, SCM, and the coupled SLUCM–SCM framework is presented in Sect. 2. In Sect. 3, we evaluate the model performance of both the SLUCM and SCM using field measurements of surface energy fluxes and vertical profiles of temperature and humidity in the ABL. The coupled SLUCM–SCM framework is then applied to study the transport of heat and moisture

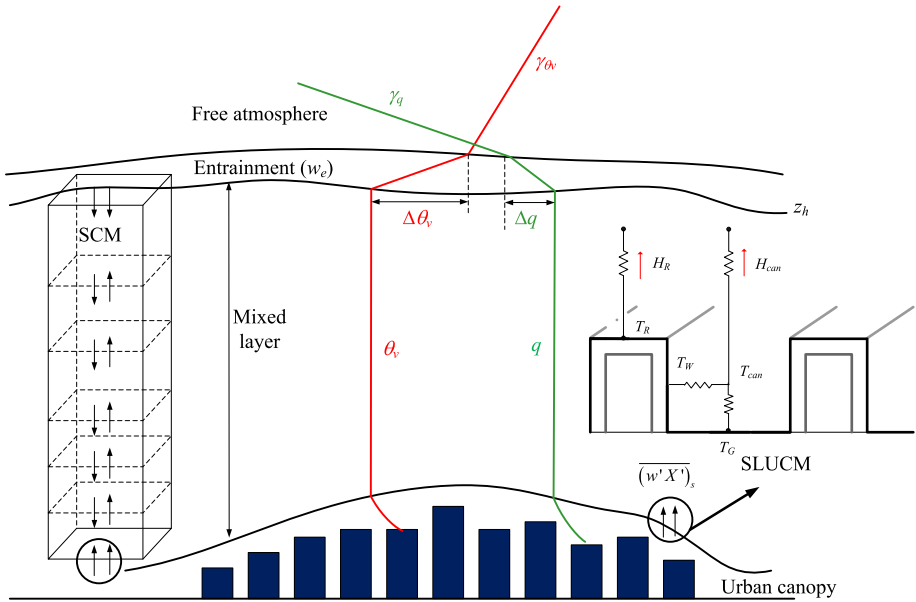


Fig. 1 Schematic of the coupled SLUCM–SCM framework: urban land-surface processes are parametrized by the SLUCM and the overlying ABL is represented by the SCM

in the integrated urban land–atmosphere system with different landscape characteristics, e.g. by changing urban geometry, surface albedo, vegetation fraction and aerodynamic roughness; results are presented in Sect. 4. The corresponding variation in ABL responses (primarily the growth of the ABL and the evolution of temperature and humidity profiles) helps to demonstrate the effectiveness of different urban planning strategies, particularly for UHI mitigation such as cool and green roofs. Lastly, the main results are summarized in Sect. 5, followed by concluding remarks.

2 Methodology

In this section, the numerical framework of the coupled urban land–atmosphere model is introduced. The urban surface layer is parametrized using the SLUCM while the overlying mixed layer is parametrized using the SCM. A schematic of the coupled SLUCM–SCM framework is shown in Fig. 1. The SLUCM–SCM framework is essentially one-dimensional with assumed horizontal homogeneity, and is appropriate for representing the ABL under free convection conditions.

2.1 Land-Surface Processes Represented by the SLUCM

To capture the coupled transport and co-evolution of water and energy budgets in a built environment, here we adopt the latest SLUCM with a realistic urban hydrological model developed by Wang et al. (2011a, 2013). The SLUCM employs the common single-layer street canyon representation for urban areas (Nunez and Oke 1977; Masson 2000; Kusaka et al. 2001) (see Fig. 1). The model explicitly resolves radiative trapping and shading effects

inside the street canyon, taking into account the canyon orientation and the diurnal variation of solar azimuth angle. Besides, surface heterogeneity for each urban facet (i.e. roof, wall, and ground) is also included: e.g. the ground can consist of, but is not limited to, engineered (asphalt or concrete) pavements, vegetation or bare soil; similarly, wall materials can be brick or glass; roofs can be paved or vegetated. Furthermore, the urban hydrological module in the SLUCM is capable of predicting water transport over both natural and engineered surfaces, especially evapotranspiration from urban lawns and water retention on porous pavements. Forced by air temperature, humidity, pressure, wind speed and shortwave and longwave radiation fluxes, the SLUCM not only predicts the surface energy balance (i.e. net radiation, surface temperature and sensible and ground heat fluxes), but also hydrological processes (infiltration, evapotranspiration and irrigation) and sub-surface soil moisture states in urban areas.

Based on the assumption that the thermal energy involved in advection, radiative flux divergence, and canyon air temperature change is small in comparison with the energy stored in urban surfaces (Nunez and Oke 1977), the energy balance in the SLUCM for the whole urban canopy layer is given by,

$$R_n + A_F = H_u + LE_u + G_0, \tag{1}$$

where R_n is the net radiation, A_F is the anthropogenic heat and moisture fluxes, H_u and LE_u are the turbulent sensible and latent heat fluxes arising from the entire urban canopy layer with the subscript u denoting the urban canopy, and G_0 is the ground (conductive) heat flux aggregated over all urban facets, taking into account the actual thickness and thermal mass of roofs, walls and ground.

The net radiation R_n for a generic urban facet (such as a roof) is calculated as

$$R_n = S^\downarrow + L^\downarrow - S^\uparrow - L^\uparrow, \tag{2}$$

where S^\downarrow and L^\downarrow are the downwelling shortwave and longwave radiative fluxes respectively, $S^\uparrow = aS^\downarrow$ is the upwelling shortwave radiative flux with a the surface albedo, and $L^\uparrow = \varepsilon\sigma T_s^4$ is the upwelling longwave radiative flux, ε is the emissivity, σ is the Stefan-Boltzmann constant, and T_s is the surface temperature. The computation of net radiation inside a street canyon involves shading and radiative trapping effects, as detailed in Sect. 4.1.

The total turbulent fluxes H_u and LE_u from the urban area can be obtained as the areal averages of the fluxes from roof and canyon, viz.

$$H_u = r \sum_{k=1}^{N_R} f_{R,k} H_{R,k} + w H_{can}, \tag{3}$$

$$LE_u = r \sum_{k=1}^{N_R} f_{R,k} LE_{R,k} + w LE_{can}, \tag{4}$$

while the canyon turbulent fluxes are aggregated from all canyon sub-facets, i.e. walls and ground, viz.

$$H_{can} = \frac{2h}{w} \sum_{k=1}^{N_W} f_{W,k} H_{W,k} + \sum_{k=1}^{N_G} f_{G,k} H_{G,k}, \tag{5}$$

$$LE_{can} = \frac{2h}{w} \sum_{k=1}^{N_W} f_{W,k} LE_{W,k} + \sum_{k=1}^{N_G} f_{G,k} LE_{G,k}, \tag{6}$$

where subscripts can, R, W, G denote street canyon, roof, wall, and ground respectively, $r = R/(R+W)$, $h = H/(R+W)$ and $w = W/(R+W)$ are the normalized (dimensionless) roof width, building height and road width respectively, with R , H and W the corresponding physical dimensions, N_R , N_W and N_G are the number of sub-facet types of roof, wall and ground, and $f_{R,k}$, $f_{W,k}$, and $f_{G,k}$ are the areal fractions of each sub-facet.

Sensible heat fluxes in the SLUCM are parametrized as (Masson 2000; Wang et al. 2013),

$$H = \frac{c_p \rho_a (T_s - T_a)}{r_a}, \tag{7}$$

for all urban facets, and latent heat fluxes are calculated from

$$LE_{eng} = \begin{cases} 0, & \text{if } \delta_w = 0 \\ \frac{\rho_a L_v (q_{eng}^* - q_a)}{r_a}, & \text{if } \delta_w > 0 \end{cases}, \tag{8}$$

for engineered surfaces, and

$$LE_{nat} = \begin{cases} \frac{L_v \rho_a (q_{veg}^* - q_a)}{r_a + r_s}, & \text{for vegetation} \\ \beta_e \frac{L_v \rho_a (q_{soil}^* - q_a)}{r_a}, & \text{for bare soil} \end{cases}, \tag{9}$$

for natural surfaces, where ρ_a is the density of the air, c_p is the specific heat capacity of the air, T_a is air temperature, δ_w is the actual depth of water retention on the engineered surface, L_v is the latent heat of water vaporization, q_a is the specific humidity of the air, q^* is the saturated specific humidity, r_a is the aerodynamic resistance calculated using Monin–Obukhov similarity theory, r_s is the stomatal resistance, and β_e is a potential evaporation reduction factor. Here, we adopt a closed-form relation proposed by Mascart et al. (1995) for r_a as functions of surface roughness and atmospheric stability. The factor β_e reflects the constraint on actual evaporation by soil water availability and can be parametrized as (Brutsaert 2005)

$$\beta_e = \frac{W - W_r}{W_s - W_r}, \tag{10}$$

where W is the volumetric soil water content, and W_s and W_r are the saturated and residual soil water content respectively. The actual soil water content can be computed by solving the Richards equation,

$$\frac{\partial W}{\partial t} = \frac{\partial}{\partial z} \left(D \frac{\partial W}{\partial z} + K + F_W \right), \tag{11}$$

where D and K are the hydraulic diffusivity and hydraulic conductivity for unsaturated soils respectively, estimated using Van Genuchten (1980), and $F_W = P + Q_F - R_o - E_T$ is the water availability term with precipitation P , anthropogenic water Q_F , surface run-off R_o , and evapotranspiration E_T .

In addition, the thermal fields in solid media, i.e. temperatures and soil heat fluxes, are computed by solving the heat conduction equation based on the Green’s function approach (Wang et al. 2011a), where thermal conductivity k and heat capacity C are needed. The anthropogenic heat and water budgets are ignored due to the lack of experimental data, but are recommended to be included whenever data are available.

2.2 Atmospheric Boundary-Layer Processes Parametrized by the SCM

The evolution of the CBL, including the boundary-layer height and spatial distributions of temperature and humidity in the mixed layer, is parametrized in the SCM. Here the thermal field in the atmosphere is described using the virtual potential temperature θ_v , accounting for the effect of water vapour and pressure on boundary-layer stability (Ouwensloot and Vilà-Guerau de Arellano 2013). For the surface layer, mean profiles of the virtual potential temperature θ_v and the specific humidity q follow approximately logarithmic law distributions, based on Monin–Obukhov similarity theory (Businger et al. 1971; Stull 1988). In the CBL, mean profiles of θ_v and q are governed by the following diffusion equation (Troen and Mahrt 1986),

$$\frac{\partial X}{\partial t} = \frac{\partial}{\partial z} (-\overline{w'X'}), \tag{12}$$

where $X = \theta_v$ or q is a generic atmospheric state variable, w is the vertical wind speed, and $\overline{w'X'}$ is the vertical kinematic eddy flux, with the overbar denoting the ensemble average.

The kinematic heat and moisture fluxes at the lower boundary of the CBL (or equivalently, at the top of the surface layer) can be derived from H_u and LE_u , as predicted by the SLUCM,

$$\left(\overline{w'\theta'}\right)_s = \frac{H_u}{\rho_a c_p}, \tag{13}$$

$$\left(\overline{w'q'}\right)_s = \frac{LE_u}{\rho_a L_v}, \tag{14}$$

where the subscript s denotes the atmospheric surface layer. From the definition of virtual potential temperature, we have

$$\left(\overline{w'\theta'_v}\right)_s = 0.61\bar{\theta} \left(\overline{w'q'}\right)_s + (1 + 0.61\bar{q}) \left(\overline{w'\theta'}\right)_s. \tag{15}$$

The upper boundary conditions at the top of the CBL are prescribed by Kim et al. (2006),

$$\left(\overline{w'\theta'_v}\right)_{z_h} = -0.15 \left(\frac{\theta_v}{g}\right) w_m^3 / z_h, \tag{16}$$

$$\left(\overline{w'q'}\right)_{z_h} \approx 0. \tag{17}$$

A conventional method used to determine z_h involves a bulk Richardson number formulation based on the assumption that continuous turbulence vanishes beyond z_h (Troen and Mahrt 1986; Zilitinkevich and Baklanov 2002),

$$z_h = \frac{Ri_{BC} U^2}{\beta \Delta\theta_v}, \tag{18}$$

where Ri_{BC} is the critical bulk Richardson number, $\beta = g/T_0$ is the buoyancy parameter with g the acceleration due to gravity and T_0 is the reference temperature, U is the horizontal wind speed at z_h , and $\Delta\theta_v = \theta_v(z_h) - \theta_s$ with θ_s calculated from

$$\theta_s = \theta_v(z_1) + \theta_T. \tag{19}$$

Here θ_T is the scaled potential temperature excess in the surface layer, given by

$$\theta_T = C \frac{\left(\overline{w'\theta'}\right)_s}{w_s}, \tag{20}$$

where C is a coefficient of proportionality (often set as 6.5 according to Troen and Mahrt 1986). The variable w_s is the velocity scale for the entire ABL, defined as

$$w_s = (u_*^3 + 7\varepsilon\kappa w_*^3)^{1/3}, \tag{21}$$

where u_* is the surface friction velocity, $\varepsilon = z_1/z_h \approx 0.1$ is the ratio of the surface-layer height to that of the ABL, κ is the von Karman constant, and w_* is the convective velocity scale given by

$$w_* = \left[\frac{g}{T_0} \left(\overline{w'\theta'} \right)_s z_h \right]^{1/3}. \tag{22}$$

Although the bulk Richardson number method outlined above is a widely used approach to estimate the boundary-layer height adopted by many numerical weather prediction models, the method is limited by the uncertainty associated with the selection of the Ri_{BC} value that varies with surface roughness and flow history and has high spatial variability (Zilitinkevich and Baklanov 2002; Jeričević and Grisogono 2006), leading to numerical instability. In this study, we adopt a recently developed analytical solution to determine z_h including the effect of moisture (Ouwersloot and Vilà-Guerau de Arellano 2013),

$$z_h = \left\{ z_{h0}^2 + \frac{(2+4w_e)}{\gamma_{\theta v}} \left[\Delta\theta_{v,0} z_{h0}^{\frac{1+w_e}{w_e}} - \left(\frac{w_e}{1+2w_e} \right) \gamma_{\theta v} z_{h0}^{\frac{1+2w_e}{w_e}} \right] \left(\hat{z}_h^{-\frac{1}{w_e}} - z_{h0}^{-\frac{1}{w_e}} \right) + \left(\frac{2+4w_e}{\gamma_{\theta v}} \right) \int_{t_0}^t \left(\overline{w'\theta'_v} \right)_s dt \right\}^{1/2}, \tag{23}$$

where z_{h0} is the initial CBL height, w_e is the entrainment rate at the inversion, $\gamma_{\theta v}$ is the lapse rate in the free atmosphere, $\Delta\theta_s$ is the potential temperature difference across the inversion, and \hat{z}_h is a correction term given by

$$\hat{z}_h = \left[z_{h0}^2 + \left(\frac{2+4w_e}{\gamma_{\theta v}} \right) \int_{t_0}^t \left(\overline{w'\theta'_v} \right)_s dt \right]^{1/2}. \tag{24}$$

Accounting for the non-local mixing and entrainment effects at the ABL top, the heat and moisture fluxes in the mixed layer can be parametrized as (Noh et al. 2003)

$$-\overline{w'\theta'_v} = K_h \left(\frac{\partial\theta_v}{\partial z} - \gamma_h \right) - \left(\overline{w'\theta'_v} \right)_h \left(\frac{z}{z_h} \right)^3, \tag{25}$$

$$-\overline{w'q'} = K_h \left(\frac{\partial q}{\partial z} - \gamma_q \right) - \left(\overline{w'q'} \right)_h \left(\frac{z}{z_h} \right)^3, \tag{26}$$

where K_h is the turbulent diffusivity. The non-local mixing terms γ_h and γ_q are parametrized by Troen and Mahrt (1986) and Noh et al. (2003)

$$\gamma_h = C \frac{\left(\overline{w'\theta'} \right)_s}{w_s z_h}, \tag{27}$$

$$\gamma_q = C \frac{\left(\overline{w'q'} \right)_s}{w_s z_h}. \tag{28}$$

Using the SCM schemes outlined above, we can then estimate the profiles of θ_v and q in the mixed layer. In addition, the following assumptions are used to obtain the spatial distributions of θ_v and q in the entrainment zone,

(a) According to [Deardorff \(1980\)](#), the thickness of the entrainment zone δ is estimated by

$$\frac{\delta}{z_h} = d_1 + \frac{d_2}{Ri_*}, \tag{29}$$

where $d_1 = 0.02$ and $d_2 = 0.05$ are empirical constants ([Noh et al. 2003](#)), and $Ri_* = (g/T_0)z_h\Delta\theta/w_*^2$ is the convective Richardson number.

(b) The heat or moisture flux in the entrainment zone is proportional to the jump in θ_v or q at the inversion ([Hong et al. 2006](#)). Specifically

$$\Delta\theta_v|_{z_h} = \overline{(w'\theta'_v)}_{z_h}/w_e, \tag{30}$$

$$\Delta q|_{z_h} = \overline{(w'q')}_{z_h}/w_e, \tag{31}$$

The entrainment rate w_e is typically in the range 0.01 to 0.2 m s⁻¹ ([Stull 1988](#)).

(c) The lapse rates γ_{θ_v} and γ_q are considered to be constant in the free troposphere above the CBL ([Kim et al. 2006](#); [Ouwensloot and Vilà-Guerau de Arellano 2013](#)).

Based on the above assumptions, the profiles of θ_v and q in the entrainment zone and the free atmosphere can be estimated as

$$\theta_v = \begin{cases} \theta_{vm} + \frac{\Delta\theta_v}{\delta}(z - z_h), & z_h < z < (z_h + \delta) \\ \theta_{vm} + \Delta\theta_v + \gamma_{\theta_v}[z - (z_h + \delta)], & z > (z_h + \delta) \end{cases}, \tag{32}$$

$$q = \begin{cases} q_m + \frac{\Delta q}{\delta}(z - z_h), & z_h < z < (z_h + \delta) \\ q_m + \Delta q + \gamma_q[z - (z_h + \delta)], & z > (z_h + \delta) \end{cases}, \tag{33}$$

where θ_m and q_m are the virtual potential temperature and specific humidity at the top of the mixed layer ([Kim et al. 2006](#)).

3 Model Evaluation

3.1 Evaluation of the SLUCM

Model predictions by the SLUCM are compared against field measurements from two eddy-covariance (EC) towers located at Phoenix, Arizona and Princeton, New Jersey, USA. Site information of the two EC towers is described in [Table 1](#) (see [Chow et al. 2014](#); [Sun et al. 2013b](#); [Ramamurthy et al. 2014](#) for more details). Meteorological forcing data used to test the SLUCM were collected from June 12–17, 2012 (all clear days) during a pre-monsoon season at Phoenix, and from May 4–9, 2010 for Princeton covering a variety of weather conditions. Results of the comparison between model predictions and field measurements are shown in [Fig. 2](#), which includes net radiation, sensible heat and latent heat fluxes. The root-mean-square errors (RMSE) for R_n, H_u, LE_u are 20, 34, 20 W m⁻² respectively for

Table 1 Geographic information of the two sites at Phoenix, Arizona and Princeton, New Jersey, USA

Experiment site	Phoenix	Princeton
Location	33.48°N 112.14°W	40.35°N 74.65°W
Measurement height (m)	22.1	23.2
Building height (m)	3.5	18.9
Land-use types	Residential	Suburban

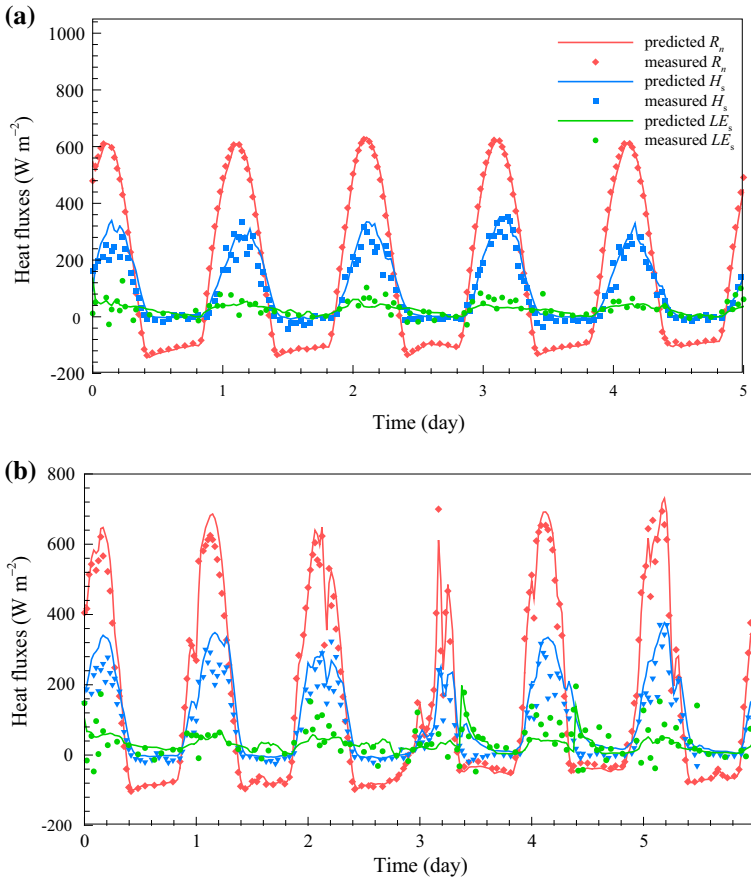


Fig. 2 Comparison of predicted sensible heat, latent heat and net radiative fluxes by the SLUCM and field measurements at **a** Phoenix, Arizona from June 12 to June 17 2012, and **b** Princeton, New Jersey from May 4 to May 9 2010

the Phoenix site, and 16, 37, 18 $W m^{-2}$ respectively for the Princeton site. It is clear that the SLUCM is capable of predicting the surface energy budget with reasonable accuracy. The realistic representation of land-surface processes by the SLUCM, especially turbulent sensible and latent heat fluxes arising from urban canopies, then provide reliable boundary conditions to the overlying CBL.

3.2 Evaluation of the SCM

To assess the SCM performance, two sets of atmospheric profiling data are used, including, (1) measurements for March 26 2005, at the Point Reyes site ($38^{\circ}5'27.6''N$, $122^{\circ}57'25.80''W$) in California, USA based on a balloon-borne sounding system (SONDE) (Atmospheric Radiation Measurement Program, 2011), and (2) Day 33 data (August 17 1967) from the Wangara experiment at Hay, New South Wales ($34^{\circ}30'S$, $144^{\circ}56'E$) (Clarke et al. 1971). Weather conditions during the measurements at both sites were highly convective, cloudless and free of synoptic frontal influences.

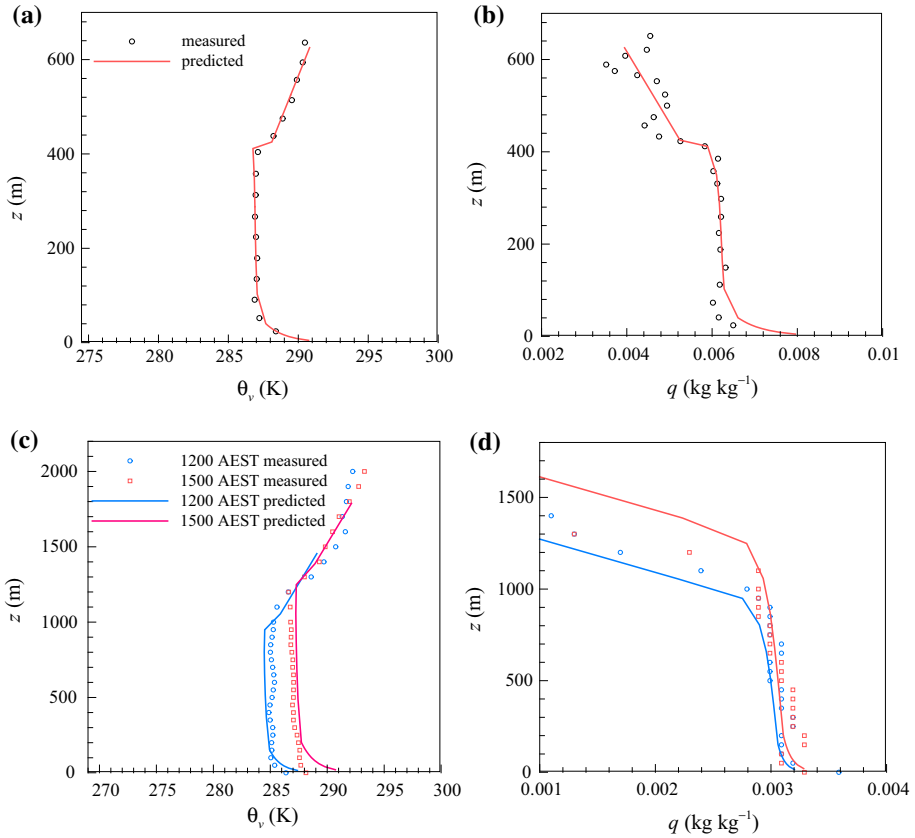


Fig. 3 Comparison of the SCM predictions and field measurements of **a** virtual potential temperature, and **b** specific humidity at 0930 PST on March 26 2005 at the Point Reyes site, California, USA, and **c** virtual potential temperature and **d** specific humidity at 1200 and 1500 AEST on Day 33 of the Wangara experiment in New South Wales, AUS

For the Point Reyes site, the surface sensible and latent heat fluxes and atmospheric temperature and humidity profiles were measured at 0930 PST (local time) on March 26 2005. The SCM is initialized with neutral virtual potential temperature and humidity profiles at the time when the CBL starts to develop (early morning). The initial values of temperature and humidity in the CBL are set to be the same as values at the top of the surface layer. Driven by the surface sensible and latent heat fluxes, the SCM determines corresponding atmospheric temperature and humidity profiles. Comparisons between predicted and measured vertical distributions of temperature and humidity in the mixed layer are in Fig. 3a, b. The *RMSE* values are 0.15 K for mean θ_v and $1.07 \times 10^{-4} \text{ kg kg}^{-1}$ for mean q in the mixed layer.

At the Wangara site, there were no direct measurements of surface sensible and latent heat fluxes. To drive the SCM, a simple “slab” model, reduced from the SLUCM without the presence of street canyons, was used to calculate these heat fluxes with the measured surface meteorological forcing, including net radiation, ground heat flux, near-surface air temperature/humidity, atmospheric pressure and wind speed. Figure 3c, d shows comparisons of the SCM predictions and measurements of θ_v and q at 1200 and 1500 AEST (local time). The *RMSE* values are 0.55 K and 0.48 K of mean θ_v in the mixed layer, and $1.02 \times 10^{-4} \text{ kg kg}^{-1}$ and $9.23 \times 10^{-5} \text{ kg kg}^{-1}$ at 1200 and 1500 AEST respectively.

It is noteworthy that, up to date, the SCM has not been tested for urban areas due to the paucity of experimental measurements of ABL profiles over built terrains. In fact, ABL profile measurements in urban areas, especially in large cities, remain a challenge because of practical difficulties associated with logistics, instrument deployment and maintenance. Nevertheless, realistic atmospheric profiles in the urban CBL can be modelled numerically, given reliable boundary conditions for the surface layer (i.e. sensible and latent heat fluxes). Thus the coupled SLUCM–SCM framework developed herein is essential to quantify the transport of energy and moisture at the interface of the urban land–atmosphere system.

4 Case Study of the Coupled SLUCM–SCM

In this section, four cases are designed to assess the impact of urban LULC changes on the atmosphere using the coupled SLUCM–SCM framework, by changing (1) street canyon aspect ratio, (2) roof albedo, (3) roof vegetation fraction, and (4) aerodynamic roughness length. Given that the SLUCM predictions are more sensitive to roof properties (Loridan et al. 2010; Wang et al. 2011b), we focus more on the effect of roof characteristics than that of the street canyon. The coupled model is driven by meteorological forcing (air temperature, pressure, humidity, wind speed, and downwelling radiation) for a sunny day (June 13 2012) in Phoenix, Arizona, with sunrise at 0518 MST (local time) and sunset at 1939 MST. The list of input parameters required by the coupled SLUCM–SCM is presented Table 2, with calibrated values from Yang and Wang (2014). Surface temperatures for different urban canyon facets (roof, wall, and ground) were initialized based on the availability of field measurements from weather stations.

4.1 Effects of Canyon-Aspect Ratio

The canyon-aspect ratio, defined as h/w , is a primary indicator of urban morphology in the SLUCM, and has a significant impact on the partitioning of radiative heat inside a street canyon (Theeuwes et al. 2014). A detailed formulation of the shortwave and longwave radiative fluxes in a street canyon, as functions of the canyon dimension, is presented in Appendix 1. Increasing h/w values imply that the morphology of a built environment changes from sparse to dense building arrays or from shallow to deep street canyons. The variation of CBL height corresponding to $h/w = 0.25, 2, \text{ and } 8$ is shown in Fig. 4a, where transition occurs at about 10.5 h after the formation of the CBL. According to Eq. 23, the evolution of CBL height is strongly related to the surface sensible heat flux as shown in Fig. 5, where a non-linear relation is found between H_s and h/w , i.e. larger h/w values lead to larger H_s in early morning and late afternoon but smaller H_s in the middle of the day. We speculate that the main contributor to this non-linear effect is the evolution of surface temperatures and heat fluxes inside the street canyon, governed by two counteracting processes, viz. the shading effect of the direct shortwave radiation and the trapping effect of diffuse shortwave radiation and longwave radiation. Schematics of the shading and trapping effects for urban canyons with different building aspect ratios are presented in Fig. 6.

To elaborate on the governing mechanisms, Fig. 7 conceptually illustrates the relationship between the change in canyon surface temperature ΔT_{can} , averaged over walls and ground, and building-aspect ratios and zenith angles. First, with the same magnitude of incoming solar radiation, canyon-aspect ratio is a significant factor in dictating ΔT_{can} . Canyons with larger h/w , i.e. taller buildings or narrower streets, tend to be warmer since more heat is trapped due to more reflections between canyon facets (trapping effect). In contrast, canyons with larger

Table 2 List of input parameters for the coupled SLUCM–SCM framework

Variable	Symbol	Value
Surface dimensional parameters		
Roof level (building height) (m)	z_R	3.5
Reference height of atmospheric measurements (m)	z_a	21.95
Normalized building height	h	0.10
Normalized roof width	r	0.45
Normalized road width	w	0.55
Roughness length for momentum above roof (m)	$z_{m,R}$	0.01
Roughness length for heat above roof (m)	$z_{h,R}$	0.002
Roughness length for momentum above canyon (m)	$z_{m,can}$	0.01
Roughness length for heat above canyon (m)	$z_{h,can}$	0.002
Surface thermal parameters		
Albedo of conventional (paved) roof	$a_{R,c}$	0.10
Albedo of vegetated roof (green-roof)	$a_{R,v}$	0.15
Albedo of wall	a_W	0.25
Albedo of ground	a_G	0.15
Emissivity of conventional roof	$\varepsilon_{R,c}$	0.95
Emissivity of vegetated roof	$\varepsilon_{R,v}$	0.93
Emissivity of wall	ε_W	0.95
Emissivity of ground	ε_G	0.95
Thermal conductivity of conventional roof ($W m^{-1} K^{-1}$)	$k_{R,c}$	0.6
Thermal conductivity of vegetated roof ($W m^{-1} K^{-1}$)	$k_{R,v}$	1.0
Thermal conductivity of wall ($W m^{-1} K^{-1}$)	k_W	1.3
Thermal conductivity of ground ($W m^{-1} K^{-1}$)	k_G	1.2
Heat capacity of conventional roof ($J m^{-3} K^{-1}$)	$C_{R,c}$	1.9×10^6
Heat capacity of vegetated roof ($J m^{-3} K^{-1}$)	$C_{R,v}$	2.1×10^6
Heat capacity of wall ($J m^{-3} K^{-1}$)	C_W	1.5×10^6
Heat capacity of ground ($J m^{-3} K^{-1}$)	C_G	1.1×10^6
Surface hydrological parameters		
Saturated soil water content (soil porosity)	W_s	0.48
Residual soil water content	W_r	0.15
Saturated hydraulic conductivity ($m s^{-1}$)	K_s	3.38×10^{-6}
Atmospheric parameters		
Entrainment rate at the inversion ($m s^{-1}$)	w_e	0.2
Lapse rate of virtual potential temperature in free atmosphere ($K m^{-1}$)	γ_{θ_v}	0.006

h/w are cooler because of a larger shaded area (shading effect). The combined effect due to h/w leads to a maximum ΔT_{can} in the moderate h/w range, as shown in Fig. 7a (Theeuwes et al. 2014). Secondly, the zenith angle of incoming solar radiation is also important for radiative trapping and shading effects. The zenith angle is directly related to, (i) the number of reflections experienced by a radiative ray inside the street canyon, and (ii) the magnitude of the incoming solar radiation depending on the time of the day. If zenith angle is close to 90

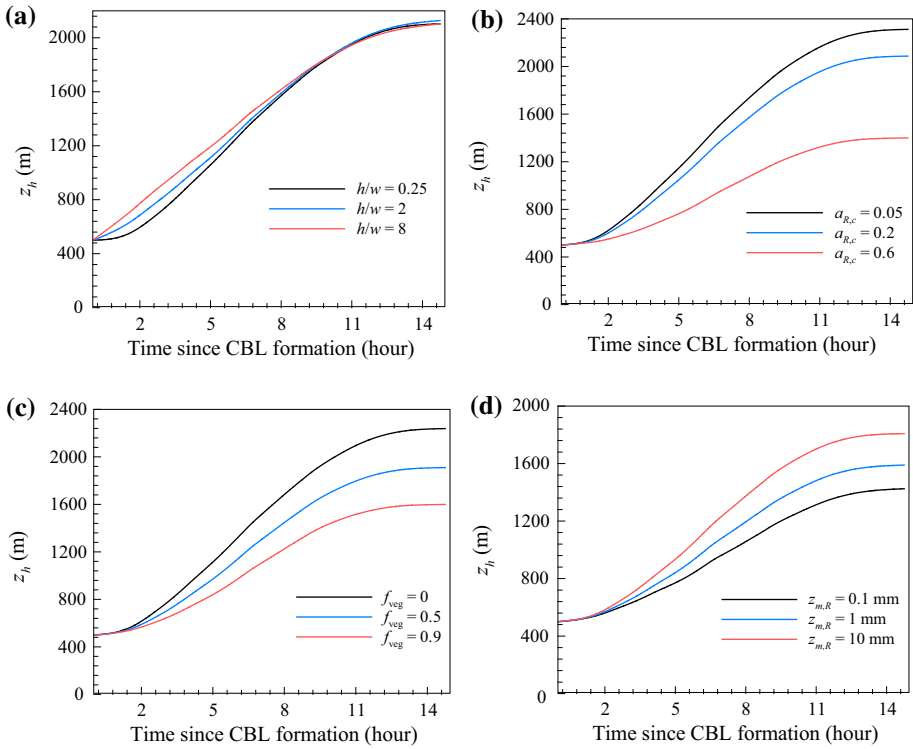


Fig. 4 Time evolution of the ABL height z_h with different land-surface characteristics: **a** aspect ratio $h/w = 0.25, 2$ and 8 ; **b** roof albedo $a_{R,c} = 0.05, 0.2$ and 0.6 ; **c** roof vegetation fraction $f_{veg} = 0, 0.5$ and 0.9 ; and **d** roof aerodynamic roughness $z_{m,R} = 0.1, 1$ and 10 mm

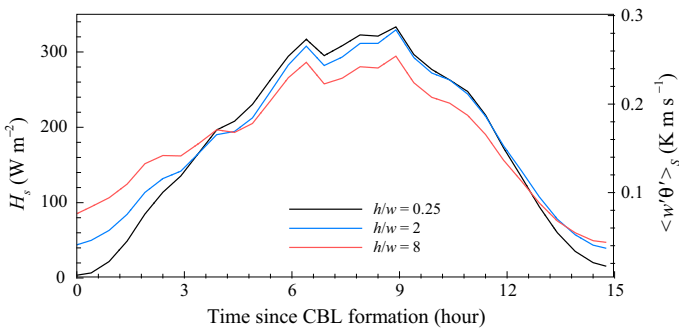


Fig. 5 Time evolution of sensible heat flux in the surface layer, H_s , for canyon aspect ratio $h/w = 0.25, 2$ and 8 , respectively. The corresponding kinematic heat flux $\langle w'\theta' \rangle_s$ values are also indicated plotted on the right (the bracket notation is used instead of overbar for the ensemble mean on the axis)

degrees, i.e. early morning or late afternoon, the trapping effect is significant due to multiple radiative reflections between canyon facets, while the shading effect is small due to low incoming solar radiation. In contrast, the street canyon exhibits a smaller trapping effect and a larger shading effect around noon when the zenith angle is close to zero. The resultant effect

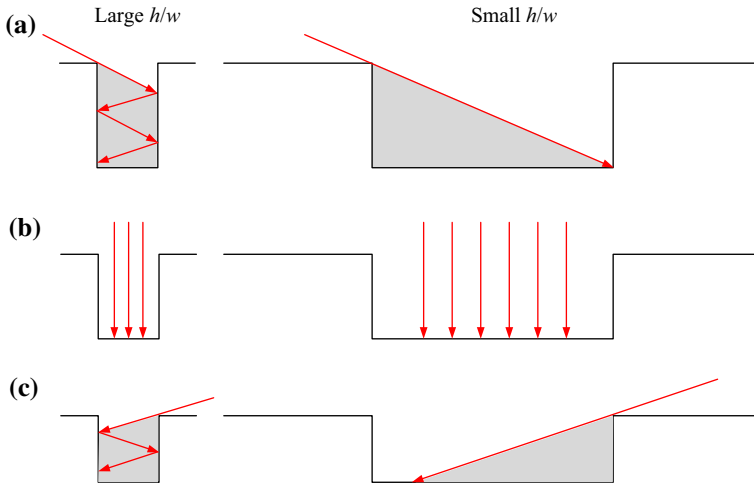


Fig. 6 Illustration of radiative trapping and shading effects in street canyons with different aspect ratios, at different time of the day: **a** early morning, **b** noon, and **c** late afternoon, with various angles of incidence of solar radiation. Note that the sketched canyon dimensions are not to scale and do not present the actual street canyons

on ΔT_{can} as a function of the zenith angle is shown in Fig. 7b. Overall, interactions between radiative trapping and shading effects lead to the non-linear effect of h/w on the sensible heat flux arising from the urban canopy during daytime (Fig. 5), which is then manifest in the diurnal evolution of the CBL height (Fig. 4a).

The effect of h/w on the spatial distribution of θ_v in the mixed layer is presented in Fig. 8. To illustrate the temporal variation of the θ_v profiles, we select six times for comparison, viz. early morning (0700 MST), late morning (1000 MST), noon (1200 MST), early afternoon (1400 MST), late afternoon (1600 MST) and dusk (1900 MST). In the morning, when the trapping effect is dominant, the canyon with $h/w = 8$ exhibits largest θ_v , while the differences among h/w cases decrease with time. This can be interpreted as the trapping effect diminishes and the shading effect becomes dominant due to the change of zenith angle. This trend continues in the afternoon until the excess temperature arising from dense urban areas (large h/w) is completely offset by the shading effect. Eventually, close to dusk, the trapping effect overtakes the shading effect again when the solar angle of incidence decreases. But the combined effect of complex radiative interactions results in the street canyon with moderate $h/w = 2$ has the highest θ_v in the mixed layer, consistent with the speculation illustrated in Fig. 7a.

4.2 Effects of Surface Albedo

Roofs with high albedo (customarily referred to as “cool roofs” in building communities) have attracted extensive interest as a popular strategy to mitigate the canopy UHI (Akbari et al. 2012; Jacobson and Hoeve 2012). However, the impact of surface albedo on the ABL over an urban area is less frequently discussed. Here we simulated three cases with different albedos of conventional (paved) roofs, viz. $a_{R,c} = 0.05, 0.2$ and 0.6 , to investigate the effect of cool roofs on the CBL temperature. Physically, higher albedo leads to lower roof surface temperature, which reduces sensible heat fluxes above the roof and the urban surface, and

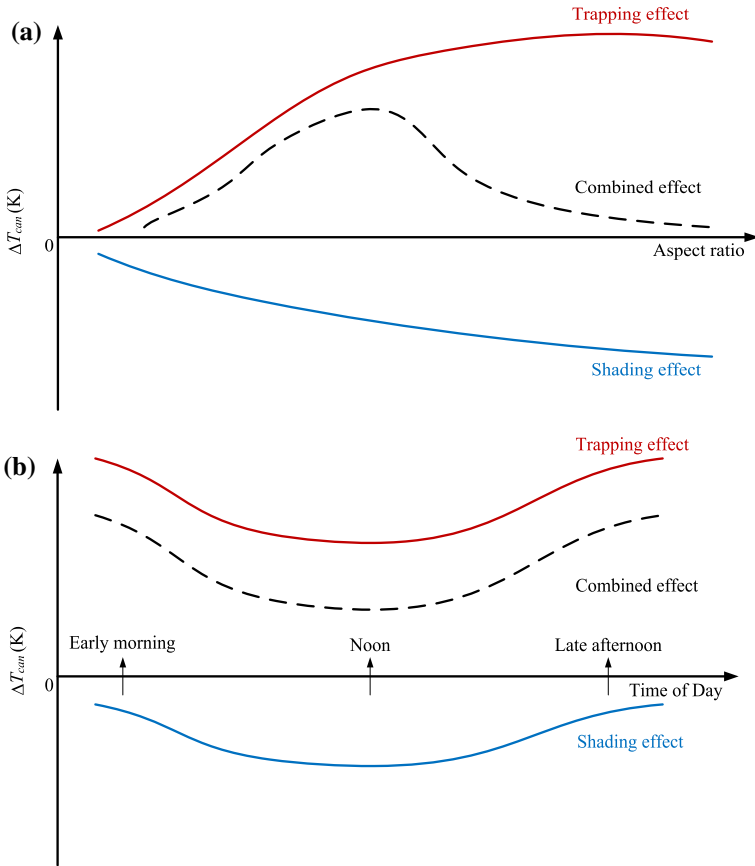


Fig. 7 Conceptual sketches of the effects of radiative trapping and shading on changes of canyon surface temperatures as a function of **a** aspect ratio, and **b** time of day

reduces the CBL height in turn, as shown in Fig. 4b. In Fig. 9, it is clear that higher $a_{R,c}$ values also result in lower θ_v in the mixed layer. Note that the simulation results in this case are based on meteorological conditions for a clear day in a desert city without clouds and aerosols in the ABL. In the presence of clouds and aerosols, the transport of shortwave and longwave radiation in the ABL, atmospheric stability and the land-surface energy partitioning are all modified (Stull 1988). Such complexities are not incorporated in the current numerical framework.

4.3 Effects of Vegetation Fraction

“Green” urban infrastructures, e.g. green roofs, urban lawns, urban agriculture, etc., are gaining increasing popularity as an effective means of reducing adverse urban environmental effects such as UHI mitigation, stormwater management and the preservation of ecological diversity (Dvorak and Volder 2010; Sailor et al. 2012; Sun et al. 2013a). Previous studies using the SLUCM have found that the vegetation fraction in built environments is critical in determining the vertical transport of heat and moisture within urban canopies (Wang et al. 2011b; Yang and Wang 2014). Using the coupled SLUCM–SCM framework, we choose

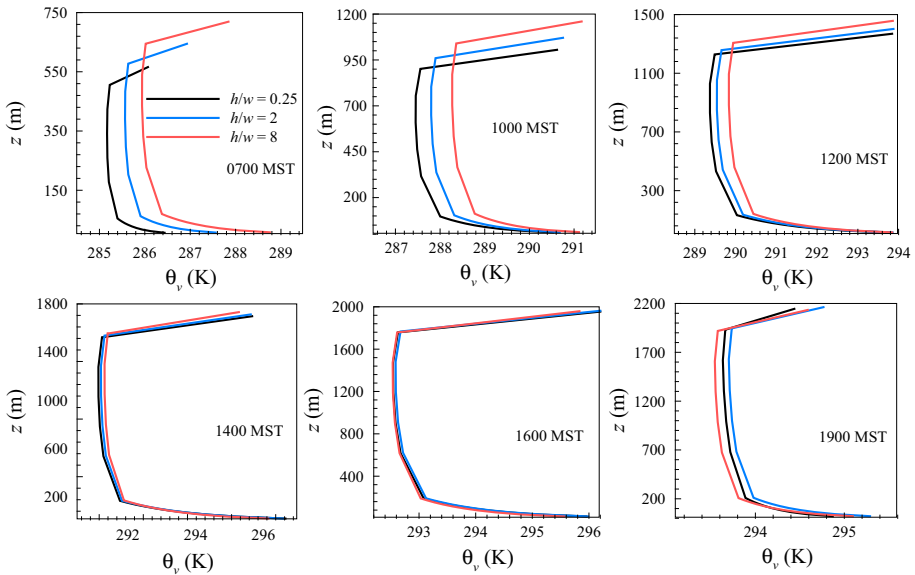


Fig. 8 Model predictions of virtual potential temperature profiles in the ABL at 0700, 1000, 1200, 1400, 1600 and 1900 MST for canyon aspect ratios $h/w = 0.25, 2$ and 8

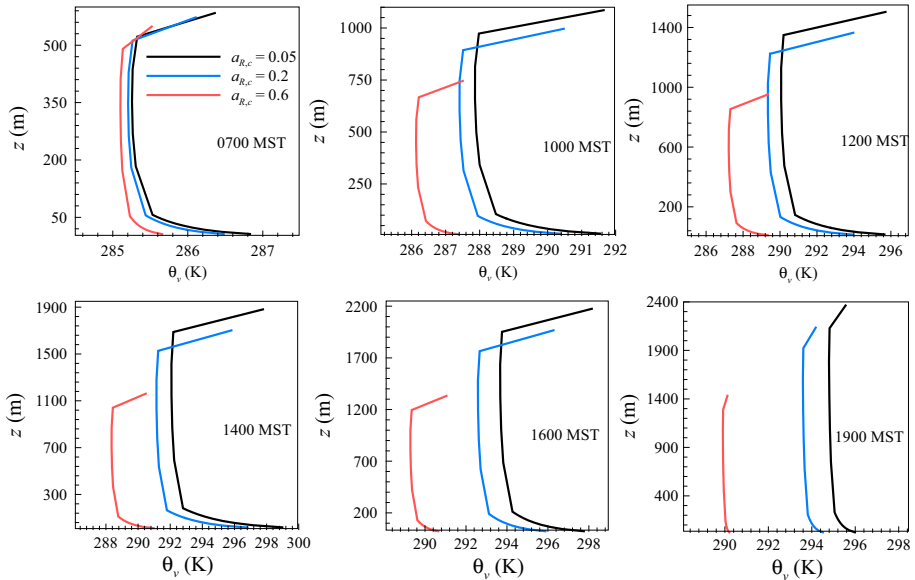


Fig. 9 Model predictions of virtual potential temperature profiles in the ABL at 0700, 1000, 1200, 1400, 1600 and 1900 MST for roof albedo $a_{R,c} = 0.05, 0.2$ and 0.6

vegetated roof fractions $f_{veg} = 0, 0.5, 0.9$ to investigate the effect of green roofs on the CBL. The growth of ABL height is presented in Fig. 4c, while the distributions of θ_v and q in the mixed layer are shown in Figs. 10 and 11, for different f_{veg} . In general, larger f_{veg} values

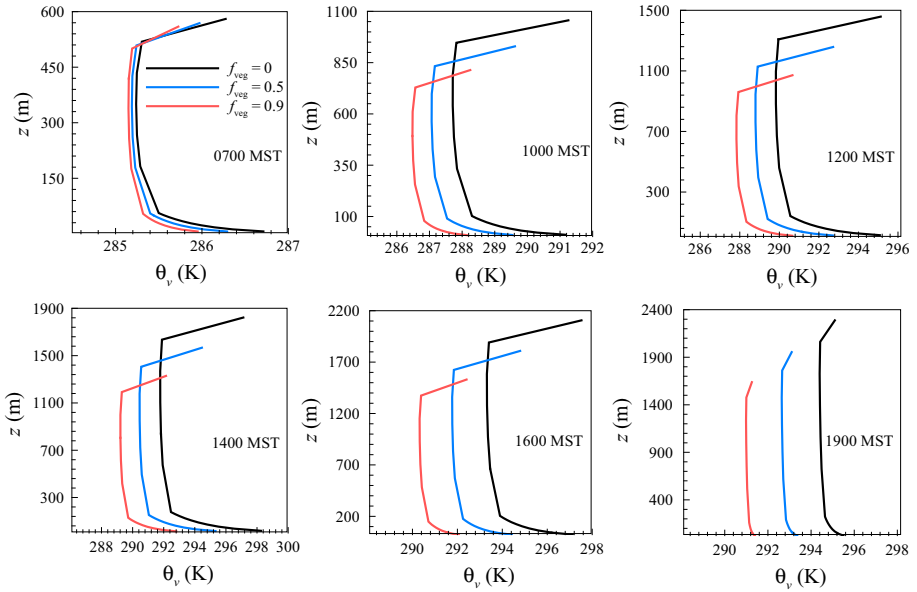


Fig. 10 Model predictions of virtual potential temperature profiles in the ABL at 0700, 1000, 1200, 1400, 1600 and 1900 MST for roof vegetation fraction $f_{veg} = 0, 0.5$ and 0.9

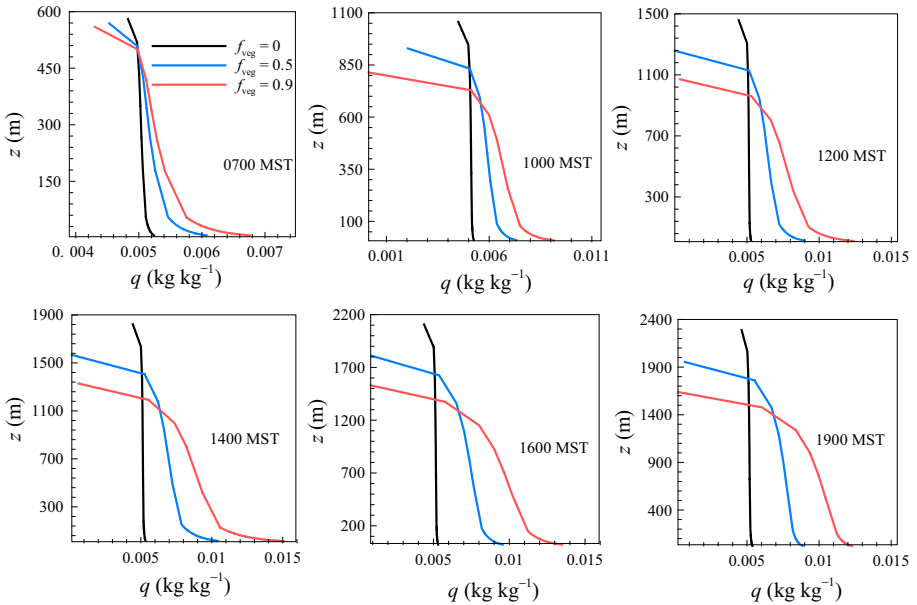


Fig. 11 Model predictions of specific humidity profiles in the ABL at 0700, 1000, 1200, 1400, 1600 and 1900 MST for roof vegetation fraction $f_{veg} = 0, 0.5$ and 0.9

lead to greater latent heat and smaller sensible heat fluxes. Consequently, an increase in green roof fraction in urban canopies results in a significant cooling effect, which can effectively “penetrate” throughout the entire CBL.

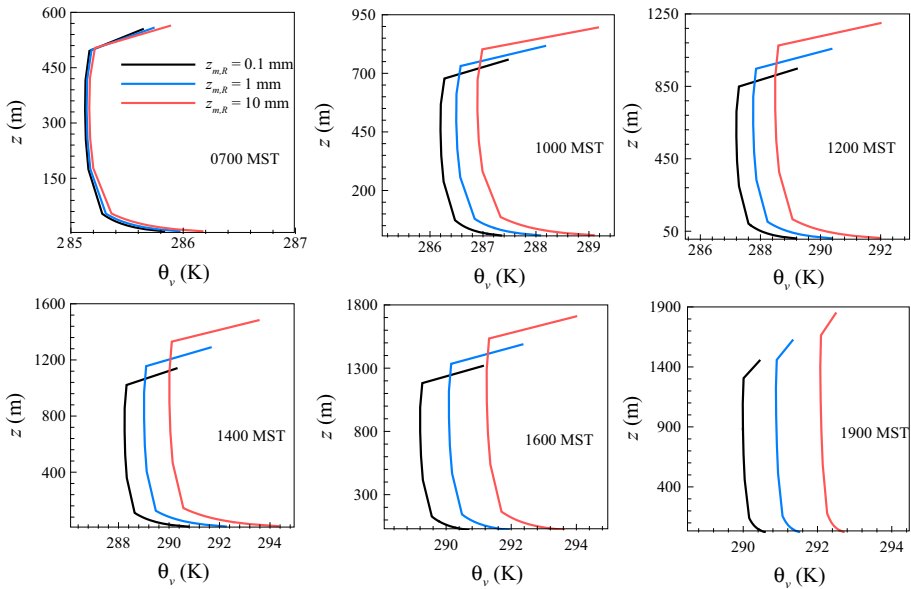


Fig. 12 Model predictions of virtual potential temperature profiles in the ABL at 0700, 1000, 1200, 1400, 1600 and 1900 MST for roof aerodynamic roughness length $z_{m,R} = 0.1, 1$ and 10 mm

4.4 Effects of Aerodynamic Roughness Length

The turbulent transport of momentum, heat and moisture in the ABL is sensitive to the surface aerodynamic roughness (Mascart et al. 1995). As shown in Eqs. 7–9, the aerodynamic resistance r_a directly affects the magnitude of sensible and latent heat fluxes. It is well-known that r_a decreases non-linearly with the surface roughness length (e.g. Stull 1988). In this case study, we modify the values of roof roughness length for momentum transfer, viz. $z_{m,R} = 0.1, 1$, and 10 mm, and investigate the same set of ABL responses (i.e. z_h and mixed-layer θ_v and q). It is expected that roofs with larger $z_{m,R}$ induce lower r_a , which in turn leads to larger H_s and LE_s due to the enhanced vertical turbulent transfer of heat and moisture. The enhanced sensible and latent heat fluxes from the surface layer then lead to higher z_h and higher θ_v and q in the mixed layer, as shown in Figs. 4d and 12 and 13. In the context of urban planning, particularly for UHI mitigation, results of this case study also demonstrate that altering roof roughness lengths is effective in regulating the transport of heat and moisture from built terrains to the overlying CBL, without fundamental changes to the urban morphology.

5 Concluding Remarks

A new SLUCM–SCM framework is developed for modelling the urban land–atmosphere interactions, with the SLUCM enabling the realistic representation of urban surface hydrologic processes including evapotranspiration, infiltration, irrigation, and sub-surface soil moisture. We test the model against field measurements of net radiation and sensible and latent heat fluxes in urban canopy layers, as well as vertical distributions of temperature and

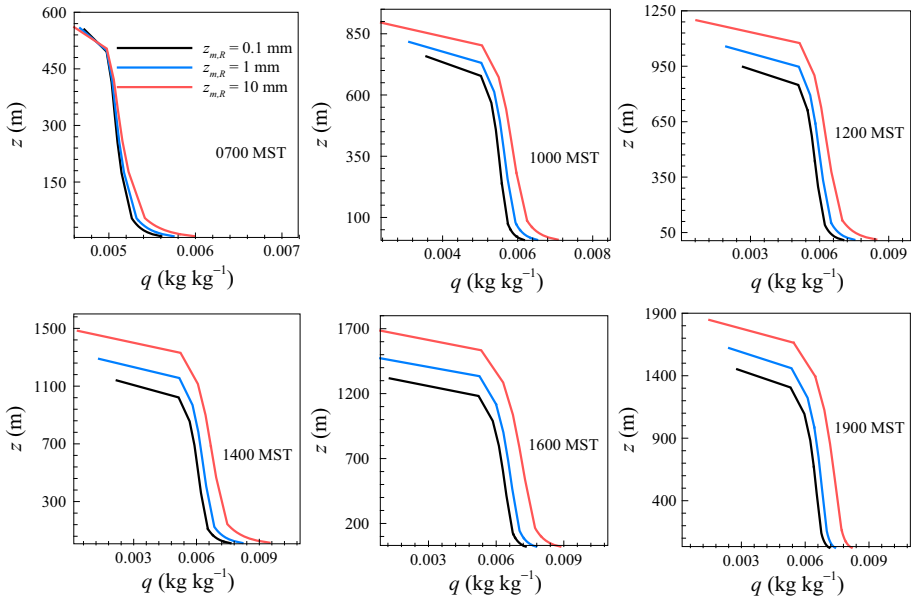


Fig. 13 Model predictions of specific humidity profiles in the ABL at 0700, 1000, 1200, 1400, 1600 and 1900 MST for roof aerodynamic roughness length $z_{m,R} = 0.1, 1$ and 10 mm

humidity and the evolution of ABL height. The coupled model is found to be robust and captures the vertical transport of heat and moisture from the surface layer to the overlying CBL via land–atmosphere interactions.

We then apply the numerical framework to study the impact of urban landscape characteristics, including morphology, albedo, vegetation fraction and aerodynamic roughness on the growth of the ABL and the distributions of temperature and humidity in the mixed layer under convective conditions. Results of case studies show that changes in land-surface properties (hydrothermal or geometric) have a significant impact on the evolution of the overlying boundary layer. In particular, the urban morphology, represented by the canyon-aspect ratio h/w , imposes non-linear effects on the ABL responses (z_h growth and θ_v distribution in the mixed layer), through rather complex interactions of the opposing radiative trapping and shading effects co-evolving throughout the daytime. It is also found that widely-used urban planning strategies especially for surface UHI mitigation, such as cool and green roofs and modification of the vertical turbulent transfer through enhanced aerodynamic conductance, are effective in influencing the transport of momentum, heat and moisture in the urban boundary layer.

Preliminary results from applications of the new SLUCM–SCM framework in the current study necessitate a few important questions for future research on urban land–atmosphere interactions. First, model uncertainties inherent in the parameter space, as well as parameterization schemes, need to be carefully quantified. With a relatively large number of input parameters, model uncertainty and sensitivity analysis necessarily requires computationally efficient numerical procedures, e.g. using advanced stochastic methods. It is also noteworthy that in the offline (stand-alone) setting, the current numerical framework has no predictive skill in the absence of projections of future atmospheric forcing. Thus it is of critical importance to run the model in an *online* setting, e.g. by incorporating the framework into numerical weather

prediction models such as the WRF model. This way, the proposed numerical framework can be driven by meteorological forcing from numerical predictions at regional scales and become predictive for scenarios of city-scale land–atmosphere interactions downscaled from future climatic projections. With land-surface processes represented by the latest SLUCM, online simulations using the coupled framework should help to provide important guidelines for future development of cities with sustainable urban planning, e.g. UHI mitigation and adaptation strategies.

Acknowledgments This work is supported by the National Science Foundation (NSF) under grant number CBET-1435881. The authors thank the Central Arizona-Phoenix Long-Term Ecological Research (CAP LTER) project under NSF grant CAP3: BCS-1026865, for partial financial support and sharing of field measurements in Phoenix. Field measurement by the Atmospheric Radiation Measurement (ARM) Program (2011) sponsored by the U.S. Department of Energy, Office of Science, Office of Biological and Environmental Research, Climate and Environmental Sciences Division is acknowledged.

Appendix 1: Calculation of Net Radiation in a Street Canyon

The net shortwave and longwave radiative fluxes for walls and ground inside a street canyon can be computed using a two-reflection model (Kusaka et al. 2001; Wang et al. 2013) as,

$$S_W = (1 - a_W) \left[S_D \frac{l_{shadow}}{2h} + S_Q F_{W \rightarrow S} + S_D \left(\frac{w - l_{shadow}}{w} \right) a_G F_{W \rightarrow G} + S_Q F_{W \rightarrow G} + S_D \frac{l_{shadow}}{2h} a_W F_{W \rightarrow W} + S_Q a_W F_{W \rightarrow S} F_{W \rightarrow W} \right], \tag{34}$$

$$S_G = (1 - a_G) \left[S_D \left(\frac{w - l_{shadow}}{w} \right) + S_Q F_{G \rightarrow S} + S_D \frac{l_{shadow}}{2h} a_W F_{G \rightarrow W} + S_Q a_W F_{W \rightarrow S} F_{G \rightarrow W} \right], \tag{35}$$

$$L_W = \varepsilon_W \left(F_{W \rightarrow S} L^\downarrow + \varepsilon_G F_{W \rightarrow G} \sigma T_G^4 + \varepsilon_W F_{W \rightarrow W} \sigma T_W^4 - \sigma T_W^4 \right) + \varepsilon_W (1 - \varepsilon_G) L^\downarrow F_{G \rightarrow S} F_{W \rightarrow G} + 2(1 - \varepsilon_G) \varepsilon_W \sigma T_W^4 F_{G \rightarrow W} F_{W \rightarrow G} + \varepsilon_W (1 - \varepsilon_W) L^\downarrow F_{W \rightarrow S} F_{W \rightarrow W} + (1 - \varepsilon_W) \varepsilon_G \sigma T_G^4 F_{W \rightarrow G} F_{W \rightarrow W} + \varepsilon_W \varepsilon_W (1 - \varepsilon_W) \sigma T_W^4 F_{W \rightarrow W} F_{W \rightarrow W}, \tag{36}$$

$$L_G = \varepsilon_G \left(F_{G \rightarrow S} L^\downarrow + 2\varepsilon_W F_{G \rightarrow W} \sigma T_W^4 - \sigma T_G^4 \right) + 2\varepsilon_G (1 - \varepsilon_W) F_{W \rightarrow S} F_{G \rightarrow W} L^\downarrow + (1 - \varepsilon_W) \varepsilon_G F_{G \rightarrow W} F_{W \rightarrow G} \sigma T_G^4 + 2\varepsilon_G \varepsilon_W (1 - \varepsilon_W) F_{W \rightarrow W} F_{G \rightarrow W} \sigma T_W^4, \tag{37}$$

where S_W and S_G are the net shortwave radiative fluxes for wall and ground respectively, L_W and L_G are the net longwave radiative fluxes for wall and ground respectively, S_D and S_Q are the direct and diffuse solar radiative fluxes, a is the albedo (solar reflectivity), $F_{i \rightarrow j}$ are the view factors for radiation emitted from a generic surface i and received by surface j , and l_{shadow} is the normalized shadow length. The shadow length is estimated by (Kusaka et al. 2001),

$$l_{shadow} = \begin{cases} h \tan \theta_z \sin \theta_n, & l_{shadow} < w \\ w, & l_{shadow} \geq w \end{cases}, \tag{38}$$

where θ_z is the solar zenith angle, θ_n is the difference between the solar azimuth angle and canyon orientation. All view factors for radiative exchange between canyon facets are directly related to the aspect ratio h/w (Wang 2010).

References

- Akbari H, Matthews HD, Seto D (2012) The long-term effect of increasing the albedo of urban areas. *Environ Res Lett* 7(2):024004
- Arnfield AJ (2003) Two decades of urban climate research: A review of turbulence, exchanges of energy and water, and the urban heat island. *Int J Climatol* 23(1):1–26
- Atmospheric Radiation Measurement (ARM) Program (2011) Balloon-borne sounding system (SONDE), sondewnpn b1 data stream. ARM Archive, Oak Ridge, TN, USA. Data subset: Oct 2010–Mar 2011, 36° 36' 18.0"N, 97° 29' 6.0"W
- Bonan GB, Oleson KW, Verstein M, Levis S, Zeng XB, Dai YJ, Dickinson RE, Yang ZL (2002) The land surface climatology of the community land model coupled to the NCAR community climate model. *J Clim* 15(22):3123–3149
- Brutsaert W (2005) *Hydrology—an introduction*. Cambridge University Press, New York 605 pp
- Businger JA, Wyngaard JC, Bradley EF (1971) Flux–profile relationships in the atmospheric surface layer. *J Atmos Sci* 28:181–189
- Chen F, Avissar R (1994) Impact of land-surface moisture variability on local shallow convective cumulus and precipitation in large-scale models. *J Appl Meteorol* 33(12):1382–1401
- Chen F, Dudhia J (2001) Coupling an advanced land surface-hydrology model with the Penn State-NCAR MM5 modeling system. Part I: Model implementation and sensitivity. *Mon Weather Rev* 129(4):569–585
- Chen F, Kusaka H, Bornstein R, Ching J, Grimmond CSB, Grossman-Clarke S, Loridan T, Manning KW, Martilli A, Miao S, Sailor D, Salamanca FP, Taha H, Tewari M, Wang X, Wyszogrodzki AA, Zhang C (2011) The integrated WRF/urban modelling system: development, evaluation, and applications to urban environmental problems. *Int J Climatol* 31(2):273–288
- Chow WTL, Volo TJ, Vivoni ER, Jenerette GD, Ruddell BL (2014) Seasonal dynamics of a suburban energy balance in Phoenix, Arizona. *Int J Climatol*. doi:10.1002/joc.3947
- Clarke RH, Dyer AJ, Brook RR, Reid DC, Troup AJ (1971) The Wangara Experiment: boundary layer data. Tech. Paper No. 19, Div Met Phys. CSIRO, Australia, p 316
- Collier CG (2006) The impact of urban areas on weather. *Q J R Meteorol Soc* 132(614):1–25
- Deardorff JW (1980) Stratocumulus-capped mixed layers derived from a three-dimensional model. *Boundary-Layer Meteorol* 18:495–527
- Dupont S, Otte TL, Ching JKS (2004) Simulation of meteorological fields within and above urban and rural canopies with a mesoscale model (mm5). *Boundary-Layer Meteorol* 113(1):111–158
- Dvorak B, Volder A (2010) Green roof vegetation for north American ecoregions: a literature review. *Landsc Urban Plan* 96(4):197–213
- Grimmond CSB, Dandou A, Fortuniak K, Gouvea ML, Hamdi R, Hendry M, Kawai T, Kawamoto Y, Kondo H, Krayenhoff ES, Lee SH, Blackett M, Loridan T, Martilli A, Masson V, Miao S, Oleson K, Pigeon G, Porson A, Ryu YH, Salamanca F, Shashua-Bar L, Best MJ, Steeneveld GJ, Tombrou M, Voogt J, Young D, Zhang N, Barlow J, Baik JJ, Belcher SE, Bohnenstengel SI, Calmet I, Chen F (2010) The international urban energy balance models comparison project: first results from phase 1. *J Appl Meteorol Climatol* 49(6):1268–1292
- Grimmond CSB, Coutts A, Dandou A, Fortuniak K, Gouvea ML, Hamdi R, Hendry M, Kanda M, Kawai T, Kawamoto Y, Kondo H, Blackett M, Krayenhoff ES, Lee SH, Loridan T, Martilli A, Masson V, Miao S, Oleson K, Ooka R, Pigeon G, Porson A, Best MJ, Ryu YH, Salamanca F, Steeneveld GJ, Tombrou M, Voogt JA, Young DT, Zhang N, Baik JJ, Belcher SE, Beringer J, Bohnenstengel SI, Calmet I, Chen F (2011) Initial results from phase 2 of the international urban energy balance model comparison. *Int J Climatol* 31(2):244–272
- Holtstlag AAM, Moeng CH (1991) Eddy diffusivity and countergradient transport in the convective atmospheric boundary-layer. *J Atmos Sci* 48(14):1690–1698
- Hong SY, Yign N, Dudhia J (2006) A new vertical diffusion package with an explicit treatment of entrainment processes. *Mon Weather Rev* 134(9):2318–2341
- Jacobson MZ, Ten Hoeve JE (2012) Effects of urban surfaces and white roofs on global and regional climate. *J Clim* 25(3):1028–1044
- Jeričević A, Grisogono B (2006) The critical bulk Richardson number in urban areas: verification and application in a numerical weather prediction model. *Tellus* 58(A):19–27
- Kim SW, Park SU, Pino D, Arellano JG (2006) Parameterization of entrainment in a sheared convective boundary layer using a first-order jump model. *Boundary-Layer Meteorol* 120(3):455–475
- Kondo H, Genchi Y, Kikegawa Y, Ohashi Y, Yoshikado H, Komiyama H (2005) Development of a multi-layer urban canopy model for the analysis of energy consumption in a big city: structure of the urban canopy model and its basic performance. *Boundary-Layer Meteorol* 116(3):395–421

- Kusaka H, Kondo H, Kikegawa Y, Kimura F (2001) A simple single-layer urban canopy model for atmospheric models: comparison with multi-layer and slab models. *Boundary-Layer Meteorol* 101(3):329–358
- Loridan T, Grimmond CSB, Grossman-Clarke S, Chen F, Tewari M, Manning K, Martilli A, Kusaka H, Best M (2010) Trade-offs and responsiveness of the single-layer urban canopy parametrization in WRF: an offline evaluation using the MOSCEM optimization algorithm and field observations. *Q J R Meteorol Soc* 136(649):997–1019
- Martilli A, Clappier A, Rotach M (2002) An urban surface exchange parameterisation for mesoscale models. *Boundary-Layer Meteorol* 104(2):261–304
- Mascart P, Noilhan J, Giordani H (1995) A modified parameterization of flux-profile relationships in the surface-layer using different roughness length values for heat and momentum. *Boundary-Layer Meteorol* 72(4):331–344
- Masson V (2000) A physically-based scheme for the urban energy budget in atmospheric models. *Boundary-Layer Meteorol* 94(3):357–397
- Niyogi D, Mahmood R, Adegoke JO (2009) Land-use/land-cover change and its impacts on weather and climate. *Boundary-Layer Meteorol* 133(3):297–298
- Noh Y, Cheon WG, Hong SY, Raasch S (2003) Improvement of the k-profile model for the planetary boundary layer based on large eddy simulation data. *Boundary-Layer Meteorol* 107(2):401–427
- Nunez M, Oke TR (1977) The energy balance of an urban canyon. *J Appl Meteorol* 16:11–19
- Ouwensloot HG, Vilà-Guerau de Arellano J (2013) Analytical solution for the convectively-mixed atmospheric boundary layer. *Boundary-Layer Meteorol* 148(3):557–583
- Ramamurthy P, Bou-Zeid E, Smith JA, Wang Z, Baeck ML, Saliendra NZ, Hom JL, Welty C (2014) Influence of sub-facet heterogeneity and material properties on the urban surface energy budget. *J Appl Meteorol Climatol* 53(9):2114–2129
- Sailor DJ, Elley TB, Gibson M (2012) Exploring the building energy impacts of green roof design decisions—a modeling study of buildings in four distinct climates. *J Building Phys* 35(4):372–391
- Skamarock WC, Klemp JB (2008) A time-split non-hydrostatic atmospheric model for weather research and forecasting applications. *J Comput Phys* 227(7):3465–3485
- Stull RB (1988) An introduction to boundary layer meteorology. Kluwer, Dordrecht 666 pp
- Sun T, Bou-Zeid E, Wang ZH, Zerba E, Ni GH (2013a) Hydrometeorological determinants of green roof performance via a vertically-resolved model for heat and water transport. *Build Environ* 60:211–224
- Sun T, Wang ZH, Ni GH (2013b) Revisiting the hysteresis effect in surface energy budgets. *Geophys Res Lett* 40:1741–1747
- Taha H (1997) Urban climates and heat islands: albedo, evapotranspiration, and anthropogenic heat. *Energy Buildings* 25(2):99–103
- Theeuwes NE, Steeneveld GJ, Ronda RJ, Heusinkveld BG, van Hove LWA, Holtslag AAM (2014) Seasonal dependence of the urban heat island on the street canyon aspect ratio. *Q J R Meteorol Soc* 140:2197–2210
- Trier SB, LeMone MA, Chen F, Manning KW (2011) Effects of surface heat and moisture exchange on ARW-WRF warm-season precipitation forecasts over the central United States. *Weather Forecast* 26(1):3–25
- Troen I, Mahrt L (1986) A simple-model of the atmospheric boundary-layer—sensitivity to surface evaporation. *Boundary-Layer Meteorol* 37(1–2):129–148
- The United Nations (UN) (2012) World urbanization prospects: the 2011 revision, New York, 33 pp
- Van Genuchten MT (1980) A closed-form equation for predicting the hydraulic conductivity of unsaturated soils. *Soil Sci Soc Am J* 44(5):892–898
- Wang ZH (2010) Geometric effect of radiative heat exchange in concave structure with application to heating of steel I-sections in fire. *Int J Heat Mass Transf* 53(5–6):997–1003
- Wang ZH, Bou-Zeid E, Smith JA (2011a) A spatially-analytical scheme for surface temperatures and conductive heat fluxes in urban canopy models. *Boundary-Layer Meteorol* 138(2):171–193
- Wang ZH, Bou-Zeid E, Au SK, Smith JA (2011b) Analyzing the sensitivity of WRF's single-layer urban canopy model to parameter uncertainty using advanced Monte Carlo simulation. *J Appl Meteorol Climatol* 50(9):1795–1814
- Wang ZH, Bou-Zeid E, Smith JA (2013) A coupled energy transport and hydrological model for urban canopies evaluated using a wireless sensor network. *Q J R Meteorol Soc* 139(675):1643–1657
- Yang J, Wang ZH (2014) Parameterization and sensitivity of urban hydrological models: application to green roof systems. *Build Environ* 75:250–263
- Yang ZL (1995) Investigating impacts of anomalous land-surface conditions on Australian climate with an advanced land-surface model coupled with the BMRC-GCM. *Int J Climatol* 15(2):137–174
- Zilitinkevich S, Baklanov A (2002) Calculation of the height of the stable boundary layer in practical applications. *Boundary-Layer Meteorol* 105(3):389–409